

# On the detection probability of neutron star glitches

M. Yu<sup>1,2\*</sup> and Q.-J. Liu<sup>3</sup>

<sup>1</sup> *National Astronomical Observatories of China, Chinese Academy of Sciences, 20A Datun Road, Chaoyang District, Beijing 100012, China*

<sup>2</sup> *Key Laboratory of Radio Astronomy, Chinese Academy of Sciences, 20A Datun Road, Chaoyang District, Beijing 100012, China*

<sup>3</sup> *Department of Astronomy, School of Physics, Peking University, Beijing 100871, China*

21 April 2017

## ABSTRACT

Neutron stars are observed to undergo small, abrupt rotational speed-up. This phenomenon is known as glitch. In pulsar timing observations, detection of a neutron star glitch is constrained by the time of occurrence of the event relative to entire observing span and observing cadences, time of occurrence of preceding/subsequent glitches relative to observing cadences and the strength of timing noise. Using the Yu et al. (2013) data sets, in this paper, we analyse the observational selection in terms of detection probability. We define partial probabilities for the constraints and use Monte Carlo method with assuming glitches distribute uniformly to solve the complete probability formula for both group case involving 157 pulsars and individual cases for each of the seven pulsars with glitch numbers  $\geq 5$ . In the simulations, numerical Bayesian inference is used for glitch identification. With the derived detection probability density and observed results, we uncover glitch size probability distribution embedded in the data for both the group and individual cases. We find the most prominent correction occurred for PSR J1341–6220, in which exponent of the power-law model varies from the observed  $+0.7_{-0.7}^{+1.4}$  to  $-0.4_{-0.4}^{+1.0}$ . We suggest observers determine the detection probability for glitch theories, e.g. the self-organised criticality.

**Key words:** stars: neutron - pulsars: general

## 1 INTRODUCTION

As the rapid co-rotation with the star, neutron star magnetosphere accelerates charged particles, generates emission and forms radiative beams. These processes make neutron stars periodic signal emitters. In an observation of a radio pulsar, received pulsar emission is integrated to increase detection significance of the pulse so as to determine its time-of-arrival (ToA). Same (or similar) observation can be carried out some time later with obtaining another ToA. This process may be repeated over years such that a series of ToAs is obtained. Intervals between two ToAs are usually not fixed but vary, e.g. from minutes, through hours to weeks. The observing cadence is dependent on artificial observing schedules. In large-scale, long-term observing programmes, a number of pulsars are thus observed, as those described by Arzoumanian et al. (1994) and Hobbs et al. (2004).

To study neutron star rotation, ToAs measured at the observatory are converted to the Solar system barycentre (a good enough inertial reference) and are then converted to rotation phases with an ephemeris (timing model). If the ephemeris has been refined and is the best, then the de-

rived phases ‘connect’ with each other<sup>1</sup>; for such a case, we say we have found the ‘timing solution’. Thus observations discretely and unevenly ‘sample’ continuous neutron star rotation. For each phase, its residual is derived as the difference between the observation and prediction (integer value) made by the ephemeris. The operations have computationally been realised with a high precision; a representative is the software package TEMPO2 (Hobbs et al. 2006; Edwards et al. 2006). As the free conversion between ToAs and rotation phases, the predicted integer phase is equivalent to idealised pulse arrival times when timing solution is established and phase residual is equivalent to timing residual. Researchers (e.g. Arzoumanian et al. 1994; D’Alessandro et al. 1995; Hobbs et al. 2010) have found, for most normal and some recycled pulsars, even with best available ephemerides, after modelling a steady stellar slowdown, timing residuals are not white noises but exhibit various random walk-like behaviours. The behaviours are

<sup>1</sup> For an idealised ephemeris, the observed phases are integers and the phase connection or coherence means the ephemeris derives right phase differences. For a practical ephemeris, phase coherence means fit for a set of ToAs with the ephemeris converges. In the pulsar community, the least-squares method has widely been used for the fit and observers have always verified solutions by eye.

\* E-mail: vela.yumeng@gmail.com, meng.yu@nao.cas.cn

known as ‘timing noise’. In power spectrum, timing noise is recognised with the feature of low frequency excess or ‘red’ such that power-law functions have been used in modelling (Coles et al. 2011; Lentati et al. 2014). Researchers (e.g. Yuan et al. 2010; Espinoza et al. 2011; Yu et al. 2013) have also found that, since a particular ToA, phases sharply grow faster than predictions and the coherence is usually (even severely) broken. This indicates a sudden increase in neutron star rotational rate, glitch, occurred sometime within the interval defined by the ToA (post-glitch first ToA) and the one before it (pre-glitch last ToA). In the literature, almost 500 glitches in hundreds of pulsars have been reported.

Observations for 165 normal pulsars between 1990 and 2011 were searched for glitches by Yu et al. (2013). At the Parkes Observatory, observing sessions were scheduled in cadences every 2–4 weeks. In each session, most member pulsars were observed for 1–10 min with a ToA obtained. Thus data spans for the pulsars ranged between 5.3 and 20.8 yr. Due to artificial changes of the observing projects, some member pulsars were not observed for some periods over the decades leaving data gaps in their ToAs. To study the evolution of neutron star rotational rate, the authors derived pulsar pulse frequencies  $\nu$  by consecutive local fits to the ToA data; number of ToAs per fit was typically five or six. Each glitch was verified by recognising a step in the frequencies  $\Delta\nu$ . To initially measure the glitch size, frequency values extrapolated with pre- and post-glitch timing solutions were compared at a glitch epoch. In many cases, the authors could not determine glitch epoch by assuming change of pulse phase at the glitch is zero. Instead they assumed glitch epochs as the mid-point between the pre-glitch last and post-glitch first ToAs with fitting for a phase shift at the assumed epoch (to assure the phase continuity). With refining measurements of glitch size and other glitch parameters by fitting ToAs around glitch with a glitch model, the authors reported out of the 165 pulsars 36 were seen to glitch and a total of 107 glitches were identified.

An interpretation for the glitch phenomenon is the avalanche release of angular momentum from neutron star inner crust superfluid when differential rotation between the superfluid and the rest of the star reaches a critical point and pinning force cannot hold the neutron superfluid vortices any more (Warszawski & Melatos 2008; Melatos et al. 2008). This view is the derivative of the phenomenon, the ‘self-organised criticality’ (Bak et al. 1988, and the references therein), that has widely been seen in nature. The self-organised criticality refers to dissipative, non-linear systems, in which ordered spatiotemporal structures develop spontaneously with sustaining an equilibrium to perturbations. It has spatiotemporal fingerprints: the spatial scale-invariant, self-similar (fractal) behaviours and the temporal  $1/f$  noise or flicker noise. In many self-organised systems, time spent in building up critical states is greater than the time scales of avalanche relaxations. Avalanches occur on all time scales, flicker noise correlates on all time scales and its power spectrum presents a power-law behaviour with roughly minus one the power exponent  $b$ . The  $1/f$  noise means a power-law distribution with exponent  $a$  of the duration (lifetime) of avalanches. So it is not noise but reflects the physics of extended dynamical systems. Concurrently avalanches occur on all self-similar spatial scales. Sizes ex-

hibit power-law distribution with exponent  $s$  and scale with lifetimes with positive power exponent  $c$ . The exponents  $s$ ,  $a$ ,  $b$  and  $c$  are related to each other through ‘scaling laws’. Correlation of spatial scales is described by a generalised Kolmogorov spectrum. Turbulence is the special case of the self-organised criticality where self-similarity occurs in both space and time.

By studying glitch size distributions of nine frequent glitching pulsars, Melatos et al. (2008) found the distributions could be fairly well modelled by power-law functions with exponents falling between  $-2.4$  and  $+0.13$ . Because glitch sizes imply spatial scales of superfluid avalanches, they suggested glitch phenomenon is a manifestation of the self-organised criticality. In addition, Melatos et al. (2008) have also found the inter-glitch times of seven (out of the nine) pulsars distributed exponentially exhibiting the evidence of Poisson processes; distributions of the other two (the Vela pulsar and PSR J0537–6910) contained Dirac components reflecting quasi-periodicities.

In principle a measurement of pulse frequency requires two ToAs. If a glitch occurs within the first or last ToA interval, we can neither verify it (by examining pulse frequencies) nor measure it (see Section 2 for details). There exists a ‘detection window’. We define it as a period which covers the entire observing time span but the first and last ToA intervals. As observations are often separated by weeks, we cannot exclude the possibility that two or more glitches occur coincidentally between two observations. The third factor that affects the detectability of glitches is researchers (e.g. D’Alessandro et al. 1995; Wong et al. 2001; Janssen & Stappers 2006) argued glitches especially small ones may ‘dissolve’ into timing noises (though this has not been quantified). These observational selection may have biased the observed statistics and our understanding to glitch mechanism. A full analysis to glitch distribution should contain both observations and detectabilities. In this work, we use the Yu et al. (2013) data sets to explore the detectability in terms of detection probability. In the following section, we describe the probability on detecting glitch events, writing down complete probability formula. Next, in Section 3, we describe our routines used for solving the probabilities. We show the results of various examinations. In Section 4, we give our solution to the complete probability formula in the form of probability density. We discuss the implications in Section 5. Then we close with a conclusion in Section 6.

Before starting, we would like to supplement two points here. First, our results are only for the Yu et al. data. For instance, same glitch may occur in the first ToA interval in our data and is undetectable but may occur in e.g. the third ToA interval in a data set with more rapid cadences and is detectable. Furthermore, white noise level might be considered when studying glitch detectability for recycled pulsars. Second, in the Yu et al. data, we have seen glitches usually exhibit several observables. Apart from the frequency step, pulse frequency first time derivative  $\dot{\nu}$  also has steps, often negative sometimes positive. Following glitches, there sometimes show exponential and/or linear recoveries (steps in  $\ddot{\nu}$ ). Despite these, out of two reasons, we have made simplification by only involving frequency step into our analysis: 1) The numerical Bayesian inference used is computationally expensive, we could not expand the dimension of parameter space further or the experiment could not be accomplished

in a reasonable time scale with our available computing facilities (see Section 4); 2) Again, frequency step is the parameter that implies avalanche spatial scale. The existence of the other observables affects the minimum detectable glitch in a given data set (see Espinoza et al. 2014, for an analysis to  $\dot{\nu}$  negative step), while we have restricted our discussion within the minimum ( $1.65 \times 10^{-9}$  Hz) and maximum ( $3.52 \times 10^{-5}$  Hz) glitches detected in the Yu et al. data.

Let us begin.

## 2 THE PROBABILITY

For a given set of ToAs, detectability of a glitch event is constrained by its occurring time (‘epoch term  $C_{\text{epoch}}$ ’), if other glitches have occurred in the same ToA interval (‘multi-glitch term  $C_{\text{multi}}$ ’) and the level of timing noise (‘noise term  $C_{\text{noise}}$ ’). Thus we can write the complete probability for a detection with size  $\Delta\nu$  as

$$P\{D(\Delta\nu)\} = \begin{cases} P\{D(\Delta\nu)|C_{\text{epoch}}\}P\{C_{\text{epoch}}\} + \\ P\{D(\Delta\nu)|C_{\text{multi}}\}P\{C_{\text{multi}}\} + \\ P\{D(\Delta\nu)|C_{\text{noise}}\}P\{C_{\text{noise}}\} & \text{within detection window} \\ 0 & \text{otherwise} \end{cases} \quad (1)$$

(where, explicitly, the constituents are assumed to be independent).

For the Yu et al. data sets, glitch size was initially measured by comparing the pulse frequencies extrapolated from pre- and post-glitch timing solutions at the assumed glitch epoch. Refined solution was obtained by fitting for the glitch model (refer to equation (1) in the Yu et al. paper) to the local data across the glitch. These fitting was realised by TEMPO2 that implements linear least-squares method (a realisation of the ‘frequentist’ method for data modelling). Although in principle two ToAs determine a pulse frequency measurement, in practice, since the observed phase samples are relative values, an arbitrary phase is involved in the fit and at least three ToAs are required in both pre- and post-glitch data span when fitting for the frequency (such that the initial evaluation for glitch size can be carried out). Therefore, we shrink the detection window by one ToA interval from both the start and the end of the entire observing time span. In other words, we re-define the detection window as the period that covers the entire observing time span but the first and last *two* ToA intervals. We also define

$$P\{C_{\text{epoch}}\} = 1 - \frac{\text{time span of the first and last two ToA intervals}}{\text{total observing time span}} \quad (2)$$

as the probability for a glitch epoch to locate in the detection window with defining

$$P\{D(\Delta\nu)|C_{\text{epoch}}\} = 1. \quad (3)$$

Now let us assume a glitch has occurred in some ToA interval (within detection window certainly) that spans  $\Delta T$ . Here comes another glitch, the probability for it to occur in the ToA interval where the first glitch is  $\frac{\Delta T}{T}$  and so

$$P\{C_{\text{multi}}\} = \begin{cases} \frac{\Delta T}{T} & \text{for coincidence} \\ 1 - \frac{\Delta T}{T} & \text{otherwise,} \end{cases} \quad (4)$$

where  $T$  is the time span of detection window. Then we define

$$P\{D(\Delta\nu)|C_{\text{multi}}\} = \begin{cases} 0.5 & \text{if coincidence} \\ 1 & \text{otherwise,} \end{cases} \quad (5)$$

though actual measurement would be dominated by the larger one if, for example, the two glitches have sizes  $10^{-5}$  and  $10^{-7}$  Hz respectively. In practice, two glitches can be resolved only if they are separated by at least three ToAs. Hence it would be better for us to expand the  $\Delta T$  by further including two ToA intervals on each side about the first glitch. For the Yu et al. data sets,  $\frac{\Delta T}{T}$  is typically  $\sim \frac{120 \text{ d}}{4000 \text{ d}}$ , which is three per cent. Then another three per cent will be multiplied to give the probability for another glitch to occur in the ToA interval where the two glitches are. This is negligible. So, for the multi-glitch term, we only consider the dual glitch case.

Finally, let us look at the noise term. The piece  $P\{C_{\text{noise}}\}$  indicates the level of (timing) noise. If (merely) a particular pulsar is studied, this piece will then be an arbitrary value and will become vanished in a normalisation process. In this case,  $P\{D(\Delta\nu)|C_{\text{noise}}\}$  forms an array (one dimensional) in which a certain member (bin) indicates the probability of detections with sizes binned to the specific size interval. For the case when a bunch of pulsars is studied, e.g. we are studying Yu et al. pulsars, the  $P\{C_{\text{noise}}\}$  piece turns to imply a distribution of noise level and,  $P\{D(\Delta\nu)|C_{\text{noise}}\}$  forms a matrix (two dimensional) in which an element (cell) indicates the probability of detections distributed into the specific size interval and noise level interval. Unlike the epoch and multi-glitch terms, the noise term cannot be determined analytically. We have run a Monte Carlo simulation to determine it. For either the individual or group case, the member detection probability is defined as the ratio of the number of detected events to the total event number distributed into the bin or cell. Results will be presented in Section 4. Next, we shall describe our numerical routines for simulating and modelling data sets, which have supported the simulation.

## 3 ROUTINES

### 3.1 Simulating and modelling data

Here, we would like to give an example, by which one can get all ideas on how have we simulated and modelled data sets. Now let us imagine we are studying a pulsar, PSR J0908–4913, a member in the Yu et al. list. We are going to simulate a set of timing residuals for it and then model the data with deriving model parameters.

We start with finding timing solution for its real ToAs. We use TEMPO2 and fit pulse frequency  $\nu$  and the first time derivative  $\dot{\nu}$  to the data to form phase-connected timing residuals. We also fit the second derivative  $\ddot{\nu}$  since the residuals further show an evident cubic structure. As we obtain phase-connected timing residuals, the pulsar ephemeris is refined. This is actually what Yu et al. have done. Then, idealised pulse arrival times are derived by simply subtracting the arrival time residuals from the ToAs. We next convert the idealised arrival times into (relative) integer pulse phases using the pulsar ephemeris. Results are recorded. With the

refined ephemeris and integer phases, we now begin to produce a simulated data set. This means we superimpose a designed residual onto each of the integer phases. As the integer phases are held fixed, even a faulty timing model can derive exact arrival time residuals and thus no phase incoherence occurs in any design. Under this principle, we firstly generate a raw time series by simply giving each integer phase a Gaussian distributed random number; uncertainty for each of the simulated ToAs takes that of the real ToA. Ingredients may be added then. One of them, an important feature for normal pulsars, is the timing noise. As described by Coles et al. (2011), a timing noise sequence and the spectrum with amplitude

$$n\sqrt{\frac{P(f)}{T}} = n\sqrt{\frac{A}{T}} \left[1 + \left(\frac{f}{f_c}\right)^\alpha\right]^{-\frac{\alpha}{4}} \quad (6)$$

form a Fourier transform pair, the power-law function  $P(f)$  is the sequence's power spectral density, which describes the 'red' feature. In the equation,  $n$  is the ToA number,  $T$  here indicates the entire time span of the data set,  $f_c$  and  $\alpha$  are spectral corner frequency and exponent respectively, and  $A$  the amplitude of the spectral density at  $f = 0$  characterising the strength of red noise. To generate red noise, we sample the (amplitude) spectrum evenly from zero frequency to Nyquist frequency ( $\frac{n}{2T}$ ) with a step size  $\frac{1}{100T}$  (one hundred times finer than the discrete Fourier transform step  $\frac{1}{T}$ ). Then the real part takes the product of the sample value and a standard Gaussian distributed random number, so does the imaginary part. We subsequently do complex-to-real Fourier transform followed by the Catmull-Rom interpolation to obtain the time series with red noise feature. To add a frequency jump  $\Delta\nu$  (glitch), we simply shift integer phases after a glitch epoch  $t_g$  by  $-\Delta\nu(t - t_g)$ . For the constant phase jump at  $t_g$ , we freeze it at zero. Up until here, the simulation is done.

Next, we shall model the simulated data with deriving model parameters. We view this problem as a 'Bayesian'. To find out the best agreement between data and model, Bayesians assess the plausibility of hypotheses (models), rather than merely deriving likelihood of data for an assumed model as frequentists do. A recent improvement for computational Bayesian inference has been made by Feroz et al. (2009) as MULTINEST, and an interface for pulsar timing analyses has been developed by Lentati et al. (2014) as TEMPONEST. We use them in this work. The problem we are studying requires to derive the posterior probability distributions for each of the parameters in the parameter space. Parameter estimates are then drawn from the posterior distributions using standard Markov Chain Monte Carlo method. According to Bayes' theorem, the posterior probability distribution is calculated as the ratio of the product of the Bayesian likelihood and the prior probability distribution to the Bayesian evidence, a normalising factor presented as the average of the likelihood over the prior. For the prior distribution of every parameter in the parameter space, MULTINEST adopts uniform distribution and we set the boundaries to well cover plausible values. We extend the parameter space with glitch epoch, glitch size, the red noise parameters (defined in equation (6)) and the white noise

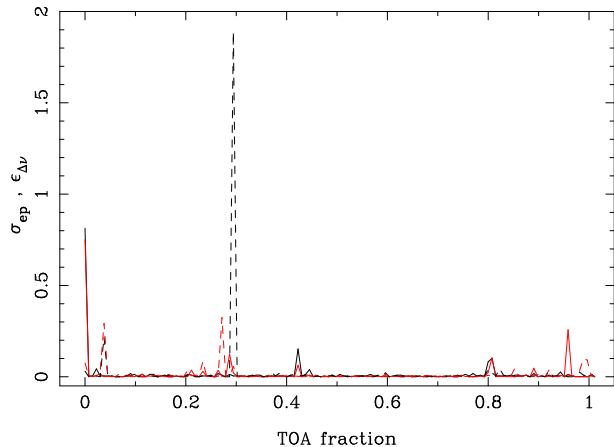


**Figure 1.** Variations of  $\sigma_{\text{ep}}$  and  $\epsilon_{\Delta\nu}$  as a function of the fraction of trial glitch epoch to the span of detection window. Black lines are for  $\sigma_{\text{ep}}$ , red lines are for  $\epsilon_{\Delta\nu}$ . Solid lines indicate test three, dashed lines indicate test four (see text).

parameters, EFAC and EQUAD<sup>2</sup>, for each flagged observing system. Since we set the phase jump at glitch epoch as zero, this term is not included into the parameter space. We marginalise all pulse parameters namely  $\nu$ ,  $\dot{\nu}$  and  $\ddot{\nu}$ . For one sampling process in the chain, MULTINEST takes a sample in the parameter space, evaluates the likelihood with the data and calculates the evidence. In likelihood evaluation, glitch is subtracted by shifting pulse phases after the sampled glitch epoch  $t_{g,s}$  by  $\Delta\nu_s(t - t_{g,s})$  where  $\Delta\nu_s$  is the sampled glitch size. The glitch search is realised in this way. Evidence calculation is computational expensive. Feroz et al. (2009) developed the ellipsoidal nested sampling method to improve the efficiency as well as the robustness, for the details, please refer to the reference. For the details on pulsar timing likelihood, please refer to Lentati et al. (2014).

### 3.2 Examinations

After describing principles of our routines, let us continue our example with some actual numbers. We would like to see if TEMPONEST may accurately return glitch epoch and size if the event is evident to eye, and if the response is uniform over the detection window. In fact, this is a point we need to examine before implementing the Monte Carlo simulation (to determine  $P\{D(\Delta\nu)|C_{\text{noise}}\}$ ). We did four tests. In test one, we simulated sets of timing residuals for PSR J0908–4913 with, 3150 d time span, 30 d (evenly) spaced ToAs and  $1 \mu\text{s}$  (fixed) ToA uncertainty. A glitch with  $\Delta\nu = 10^{-7}$  Hz was added for each realisation with trial glitch epoch moving across the detection window at step 30 d. We introduce  $\sigma_{\text{ep}}$ , absolute difference between returned glitch epoch and input epoch over average ToA interval, and

<sup>2</sup> These parameters are designed for artificially changing ToA uncertainty to study two white noise components. The EFAC accounts for man-made sources, e.g. the various radiometer noise level of observing systems. The EQUAD accounts for pulsar intrinsic sources, e.g. the 'jitter' phenomenon (Liu et al. 2012). Please refer to equation (10) in Lentati et al. (2014) for ToA uncertainty with the EFAC and EQUAD adopted in TEMPONEST.

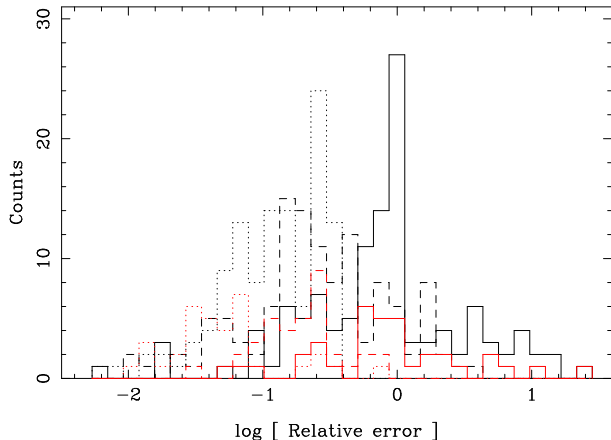


**Figure 2.** Histogram (32 bins) of spectral parameters’ relative errors which are from the examination to TEMPONEST red noise modelling. Solid bars are for  $A$ , the amplitude of power spectral density. Dashed bars are for  $f_c$ , the spectral corner frequency. Dotted bars are for  $\alpha$ , the spectral exponent. Black is for the 121 pulsars that were not seen to glitch in the Yu et al. sample, while red is for the observed 36 glitching pulsars.

relative size error  $\epsilon_{\Delta\nu}$ , absolute difference between returned glitch size and input size over input size, to characterise the accuracy of the returned values respectively. Results showed  $\sigma_{\text{ep}}$  values were consistent with zero to at least seven decimal places,  $\epsilon_{\Delta\nu}$  values were consistent with zero to at least six decimal places. Then, in test two, we moved toward reality by introducing real observing sampling (the observed, refined integer phases) and ToA uncertainties into the simulation to timing residuals. A glitch also with  $\Delta\nu = 10^{-7}$  Hz was moved across the detection window by an average ToA interval (23 d) over realisations. Results showed both  $\sigma_{\text{ep}}$  and  $\epsilon_{\Delta\nu}$  values were consistent with zero to at least two decimal places. Then, in test three, we further added timing noise to the simulated timing residuals. For the spectral parameters (see equation (6)), we adopted  $f_c = 0.06 \text{ yr}^{-1}$ , the reciprocal of the observing time span,  $\alpha = 4.0$ , the limit of the steepness for first order pre-whitening to overcome ‘spectral leakage’ (Coles et al. 2011), and  $A = 1.0 \times 10^3 \text{ s}^3$ , an arbitrary strength to which a  $\Delta\nu = 10^{-7}$  Hz glitch is well identifiable by eye. In Figure 1, we plot the variations of  $\sigma_{\text{ep}}$  and  $\epsilon_{\Delta\nu}$  with respect to the fraction of trial glitch epoch within the detection window. As another check, we, in test four, changed  $A$  to  $1.0 \times 10^8 \text{ s}^3$  and  $\Delta\nu$  to  $10^{-5}$  Hz. Results are also plotted in Figure 1. The largest  $\sigma_{\text{ep}} \sim 1.9$  was found in test four but it is still smaller than 3.0, the criterion for resolving two glitches. Most  $\sigma_{\text{ep}}$  values are consistent with zero to two decimal places. For the largest  $\epsilon_{\Delta\nu} \sim 0.75$  occurred in test three, the size returned is away within a factor of two. Most  $\epsilon_{\Delta\nu}$  values are consistent with zero to two decimal places.

The other point we ought to examine is how well TEMPONEST models red noise. This is essentially required before we determine  $P\{C_{\text{noise}}\}$ . In this examination, we no longer involved only an individual pulsar but enlarged our sample by including as many as Yu et al. pulsars if phase-connected timing solutions could be obtained over entire data spans. We thus involved 157 pulsars, all 36 observed glitching pulsars were included. For the other eight, there commonly exist

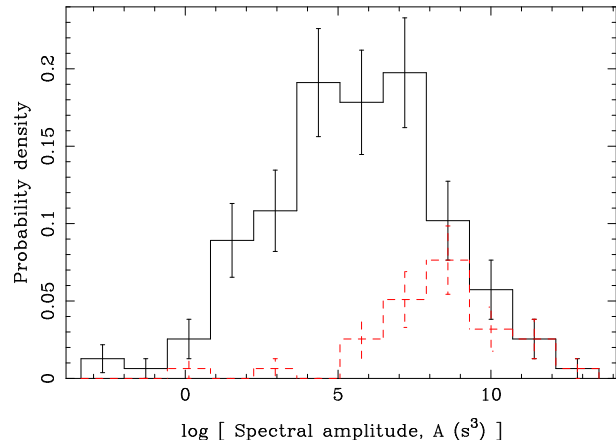


**Figure 3.** Probability density of the amplitude of power spectral density of 157 pulsars in the Yu et al. sample,  $P\{C_{\text{noise}}\}$  (12 bins). Red dashed bars indicate contribution of the 36 observed glitching pulsars.

large data gaps for typically thousands of days (and overall timing solutions were not obtained)<sup>3</sup>. Our scheme for this examination was to model simulated red noise for each of the 157 pulsars. In the simulations, real observing sampling and ToA uncertainties were used. For the input spectral parameters, as in last examination, we took the reciprocal of the observing time spans for corner frequencies, and we fixed exponents at 4.0 for all pulsars. But we no longer arbitrarily set noise strength. For a given pulsar with timing residuals  $r_i$  ( $i = 0, 1, \dots, n$ ), we roughly estimated the amplitude of the power spectral density  $A$  as

$$\frac{T}{n^2} \sum_i r_i^2 \sim \frac{T}{n} \text{rms}^2 \sim T \cdot \text{rms}^2, \quad (7)$$

or the product of the observing time span and the mean-square residual. In the equation, the summation over  $r_i$  squares is the standard deviation of the power spectrum of a white noise sequence (Ransom et al. 2002). (So we call this estimate ‘rough’.) As in last examination, we use relative error to characterise the accuracy of returned values. We did one realisation for each pulsar. Figure 2 shows the histogram of the relative errors of the spectral parameters. We found, out of the  $157 \times 3$  measurements, 412 (87.5%) had a relative error smaller than 1.0. In particular, for the measurements of  $A$ , this proportion was 114/157. After the examinations, we moved on to fit red noises for real data.

## 4 SOLUTION

### 4.1 Noise term

With the awareness of the performance of TEMPONEST red noise modelling, we fitted red noises for the 157 pulsars. In Figure 3, the top panel shows  $P\{C_{\text{noise}}\}$ , the probability density of the amplitude of power spectral density  $A$ , derived

<sup>3</sup> The eight pulsars are PSRs J1016–5819, J1327–6400, J1524–5625, J1541–5535, J1637–4642, J1821–1419, J1853–0004 and J1853+0011.

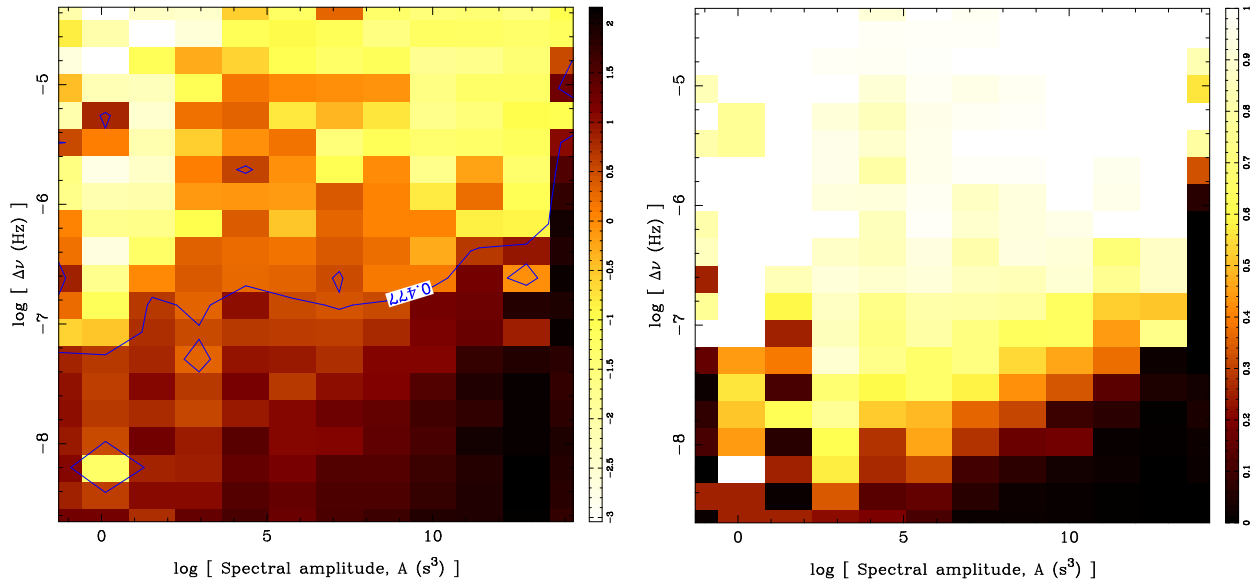


**Figure 4.** Left panel: The  $12 \times 20$  grid showing  $\sigma_{\text{ep}}$  variations as a function of timing noise strength and glitch size. The contour is at  $\sigma_{\text{ep}} = 3.0$ . Pixel values are in logarithmic scale. Right panel: Same grid showing the solution to the  $\text{P}\{D(\Delta\nu)|C_{\text{noise}}\}$  matrix. Each cell indicates the ratio of the number of positive detections to the total number of glitches distributed into the cell. To present the image clearer, value for each pixel is squared.

by normalising the various counts to the binned logarithmic amplitude values. Uncertainties were determined as the square root of the counts followed by the same normalisation. As our sample is not large, the bin number twelve is the largest that avoids a void bin. It shows that high end of the distribution is more contributed by the pulsars that have been observed to glitch (than by the pulsars otherwise). This could be because unmodelled glitch features have caused red noises.

After we measured spectral parameters, we were able to run the Monte Carlo simulation to determine  $\text{P}\{D(\Delta\nu)|C_{\text{noise}}\}$ . In total, we made 100 realisations for each pulsar. In each of the realisations, a glitch event with an epoch uniformly distributed within the specific detection window and a size uniformly distributed between  $1.65 \times 10^{-9}$  and  $3.52 \times 10^{-5}$  Hz (exclusive) was added into the simulated timing residuals; size boundaries were defined by the minimum and maximum detected sizes in the Yu et al. data. Before adding a glitch, real pulsar ephemeris, observing sampling, ToA uncertainties and the measured spectral parameters were used to produce residuals. Although more realisations might be desirable, we were restricted by the expensive computation of running the MULTINEST at double-double precision. The option of the high precision was to robustly calculate the Bayesian evidence. Its value, for some cases, has expanded up to a few thousand in logarithmic scale. In practice, such an integration has required an Intel<sup>®</sup> 2.5GHz processor to take hours to complete and, for model evaluation, tens of sampling (to the parameter space) were typically made. Difficulties in the evidence evaluation have been fully interpreted by Ferroz et al. (2009).

As in Section 3.2,  $\sigma_{\text{ep}}$  can be the index for glitch location. We scatter the obtained 15,700  $\sigma_{\text{ep}}$  values onto a plane. One dimension denotes strength of timing noise, one dimension denotes size of glitches. To illustrate, we average

the values scattered into the same cell, as shown in Figure 4 left panel. The twelve-by-twenty grid was chosen such that none of the cells is empty. It is natural to see that it is easier to detect glitches with larger sizes in weaker timing noises. We then draw a contour at 3.0 to illustrate the criterion for ‘positive’ detections. In other words, we define those detections with  $\sigma_{\text{ep}} < 3.0$  as ‘positive’, the others are ‘negative’. Under this definition, we derive the detection probability for each cell on this plane ( $\text{P}\{D(\Delta\nu)|C_{\text{noise}}\}$ ) as the ratio of the number of positives to the number of the total scattered into the cell. In Figure 4, the right panel illustrates this matrix. In fact, this figure was expected to present the same pattern as the left panel. For each element in the matrix, uncertainty was determined via square root of the counts and error propagation. Now, we do product for the matrices  $\text{P}\{D(\Delta\nu)|C_{\text{noise}}\}$  and  $\text{P}\{C_{\text{noise}}\}$  followed by a normalisation to derive solution of the noise term. Result is given in Figure 5.

## 4.2 Epoch term and multi-glitch term

After solving for the noise term, we implemented equations (2) to (5) to derive  $\text{P}\{D(\Delta\nu)|C_{\text{epoch}}\}\text{P}\{C_{\text{epoch}}\} + \text{P}\{D(\Delta\nu)|C_{\text{multi}}\}\text{P}\{C_{\text{multi}}\}$  for each of the glitches simulated. Then we scattered the values into the twenty  $\Delta\nu$  bins, made sum in each bin and did normalisation. Uncertainty for each bin was determined as the square root of the bin value followed by the same normalisation. It had been expected that the distribution would be uniform as we uniformly generated  $\Delta\nu$  values and scattered them uniformly. Result plotted in Figure 5 confirms this. The low at the boundaries reflects the fact that we generated  $\Delta\nu$  values in the open interval. Finally, we added the partial detection probability densities of the epoch, multi-glitch and noise terms in each  $\Delta\nu$  bin together and made normalisation to obtain solution

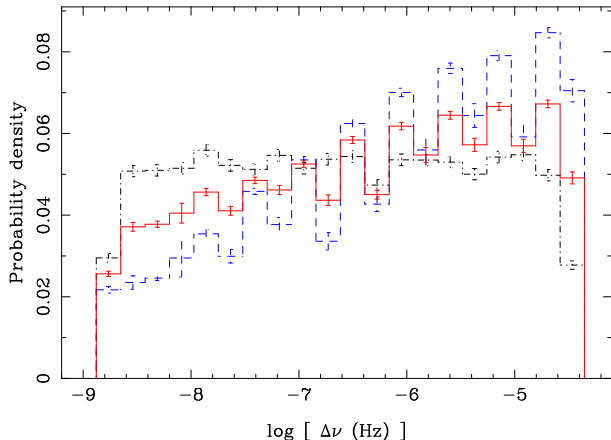


**Figure 5.** Solution of glitch detection probability as a function of glitch size presented in the form of probability density (20 bins). Blue dashed bars indicate the noise term, black dashed-dotted bars indicate the epoch and multi-glitch terms and red solid bars indicate the complete probability.

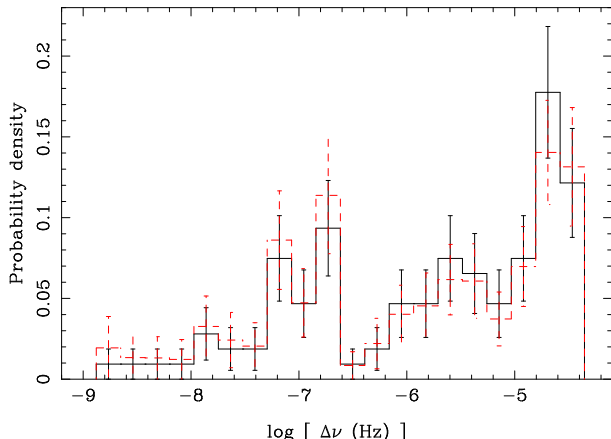


**Figure 6.** The apparent (black solid) and the inferred (red dashed) aggregated glitch size distribution.

for the complete probability formula (equation (1)). Uncertainty for each bin was determined by error propagation and the same normalisation. Result is plotted in Figure 5. We see that detectability of glitches is not uniform with respect to glitch sizes, the detection probability density becomes more and more massive as glitch becomes large. Fluctuations result from the finite scale of our simulation.

## 5 DISCUSSION

### 5.1 Aggregated distribution

With the detection probability densities derived, we are able to infer the aggregated glitch size distribution embedded in the Yu et al. data sets. In the histograms in Figure 6, the solid bars present the observed distribution. We divide the observations by the detection probability densities. After a normalisation, we present the result with the dashed bars. We see that the inferred distribution appears similar to the observed distribution. This means most glitches

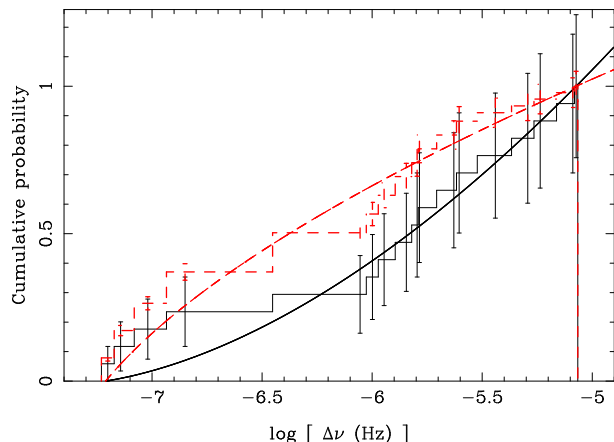
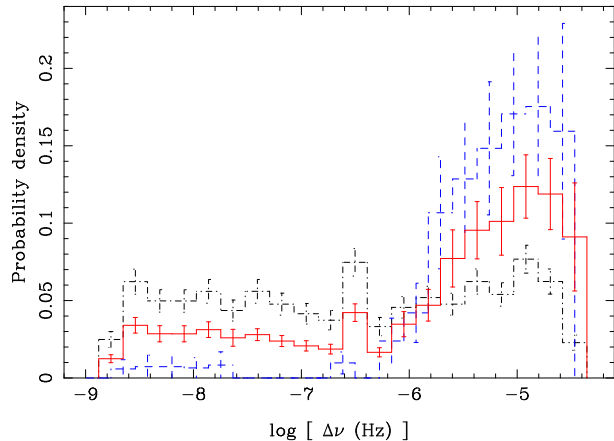


**Figure 7.** Upper panel: Glitch detection probability densities of PSR J1341–6220. Blue dashed bars indicate the noise term, black dashed-dotted bars indicate the epoch and multi-glitch terms and red solid bars indicate the complete probability. Binning is the same as Figure 5. To present the histograms clearer, the black dashed-dotted and red solid bars are shifted right by half bin size. Lower panel: The observed (black solid) and inferred (red dashed) cumulative distribution of glitch sizes for PSR J1341–6220. Curves are the fitted power-law models (see text).

embedded in the data sets are detectable. Using the manual searching method Yu et al. have detected the glitches that could be detected. The similarity also means we have set up a good model for glitch detectability of the data sets and manual method. However, when we observe the distributions more carefully, we find the inferred distribution becomes a bit more massive than the observed one for glitches with  $\Delta\nu \lesssim 4 \times 10^{-7}$  Hz, implying Yu et al. were unable to detect some small glitches. This would result from the lower detectability for small glitches of the data sets. To study this in more detail, next, we shall determine the detection probability densities for each of the pulsars PSRs J1048–5832, J1341–6220, J1413–6141, J1420–6048, J1740–3015, J1801–2304 and J1801–2451; they are the pulsars that have glitch numbers  $\geq 5$  in the data.

## 5.2 Individual distributions

Among the seven pulsars PSR J1341–6220 was observed to show seventeen glitches from MJD 49540 to MJD 55461, presenting the largest glitch number and highest glitching rate. We study it first. Similar to the group study we used the Monte Carlo method to solve the complete probability formula (equation 1). We recall the description in Section 2 that the only difference of the probability definition for individual case from group case is the  $P\{C_{\text{noise}}\}$  piece is an arbitrary number rather than a distribution. We thus made it one. In each realisation, real pulsar ephemeris, observing sampling, ToA uncertainties and the measured power spectral parameters were used to generate timing residuals; a glitch with epoch uniformly distributed within the detection window and size uniformly distributed between  $1.65 \times 10^{-9}$  and  $3.52 \times 10^{-5}$  Hz (exclusive) was then added into the simulation. TEMPONEST was used for the glitch search, parameter space was defined in the same way as in the group study. Detections satisfying  $\sigma_{\text{ep}} < 3.0$  were recognised as positive. Up until the final preparation for this section, we accumulated 482 realisations. In Figure 7 the upper panel gives the derived detection probability densities; uncertainties were determined in the same way as in the group study. We see that the densities vary around 0.02 up until  $\Delta\nu \sim 10^{-6}$  Hz, then the densities grow to around 0.1. In other words the probability for detecting a glitch with  $\Delta\nu \lesssim 10^{-6}$  Hz is about three times smaller than the probability for detecting a glitch with  $\Delta\nu \gtrsim 10^{-6}$  Hz. This would cause bias in our knowledge of the pulsar’s glitch size distribution. In Figure 7 lower panel the solid bars present cumulative distribution function (CDF) of the glitch sizes observed in PSR J1341–6220; uncertainty for each bin was determined as square root of the count followed by the same normalisation. We least-squares modelled the CDF using the function

$$P(< \Delta\nu) = \frac{\Delta\nu^{1+s} - \Delta\nu_{\min}^{1+s}}{\Delta\nu_{\max}^{1+s} - \Delta\nu_{\min}^{1+s}} \quad (8)$$

with fixing  $\Delta\nu_{\min}$  and  $\Delta\nu_{\max}$  at the minimum and maximum glitch sizes observed in the pulsar respectively. We obtained  $s = 0.7_{-0.7}^{+1.4}$ . The following Kolmogorov-Smirnov (K-S) test gave  $Q_{KS} = 0.20$  the probability that the null hypothesis, the data and model are drawn from the same distribution, is false. Uncertainties for  $s$  were determined as the boundaries of 68 per cent confidence level to reject the null hypothesis. To infer the glitch size distribution embedded in the data with the observed distribution and derived detection probability densities, we first binned the observed  $\Delta\nu$  values into the twenty density bins; for bin  $i$ , count is denoted  $m_i$ . Then we picked up those bins with  $m_i > 0$ . When forming the inferred CDF we used the nearest integer of  $m_i/p_i$  ( $p_i$  is the density value of bin  $i$ ) instead of one as the step at each  $\Delta\nu$  value. Uncertainty for each bin was determined via error propagation. Result is plotted in Figure 7 lower panel as dashed bars. K-S test gave  $Q_{KS} = 0.10$  when comparing the data with the model with an exponent  $s = -0.4_{-0.4}^{+1.0}$ . This verifies our argument that the low detectability for small glitches of the data has biased our knowledge of PSR J1341–6220’s glitch size distribution.

After analysing PSR J1341–6220 the same routine was implemented for the other six pulsars each. Up until the final preparation of this section, 294 realisations were ob-

tained for PSR J1048–5832, 209 for PSR J1413–6141, 201 for PSR J1420–6048, 200 for PSR J1740–3015, 200 for PSR J1801–2304 and 195 for PSR J1801–2451. In Figure 8 we present their glitch detection probability densities. The lower detectabilities of small glitches ( $\Delta\nu \lesssim 10^{-7}$  Hz) are commonly seen in the solutions of the noise term. The small scale of the simulations results in large fluctuations in the solutions of the epoch and multi-glitch terms and in the solutions of the complete probability. In Figure 9 CDFs of the observed glitch sizes for every pulsars are plotted as solid bars, CDFs inferred with the detection probability densities and observations are plotted as dashed bars. Table 1 gives results of the K-S tests. We see the corrections to the observed CDFs with taking the detection probability densities into account are insignificant for these cases. Therefore we can say the power exponents measured are the values drawn from the data.

## 5.3 Significance for the avalanche model

As described in Section 1, the avalanche model or the general self-organised criticality expects power-law distributions for glitch sizes. Warszawski & Melatos (2008) and Melatos et al. (2008) suggested the exponent is a function of physical quantities e.g. stellar temperature and strength of pinning forces etc. Therefore it becomes an essential requirement for observers to determine the detection probability densities for glitch events (such that power exponent embedded in the data can be drawn).

However glitches have been found to violate scale-invariance. By analysing the data set with high observing cadences for the Crab pulsar, Espinoza et al. (2014) found the smallest glitch detected was well above the minimum detectable glitch size defined by the data set. They concluded the Crab pulsar has a glitch size lower cut-off.

Glitch temporal behaviour is another point to compare with the self-organised criticality. In Figure 10 we present the Lomb normalised periodogram (Lomb 1976; Scargle 1982) of the glitch time series, the variation of glitch size as a function of glitch epoch, of the seventeen glitches observed in PSR J1341–6220. In making it, we sampled the spectrum four times finer than at the conventional interval, reciprocal of the time span, and derived the spectrum up until two times the Nyquist frequency. We see, in logarithmic space, the power demonstrates a tendency of increasing as frequency increases. Although the derived detection probability densities (Figure 7 upper panel) tell us we do not have the glitch time series embedded in the data, the observed series do have manifested the low-frequency (relative to the data span) characteristic of the pulsar’s glitch time series. A least-squares fit to the periodogram showed the slope, so that the power exponent, is  $b = 0.5(3)$ . This is far from  $-1$  the value of flicker noise. Our analysis shows glitch temporal behaviour is not in agreement with the self-organised criticality.

## 6 CONCLUSION

In this work, we studied observational selection of neutron star glitches in terms of detection probability using

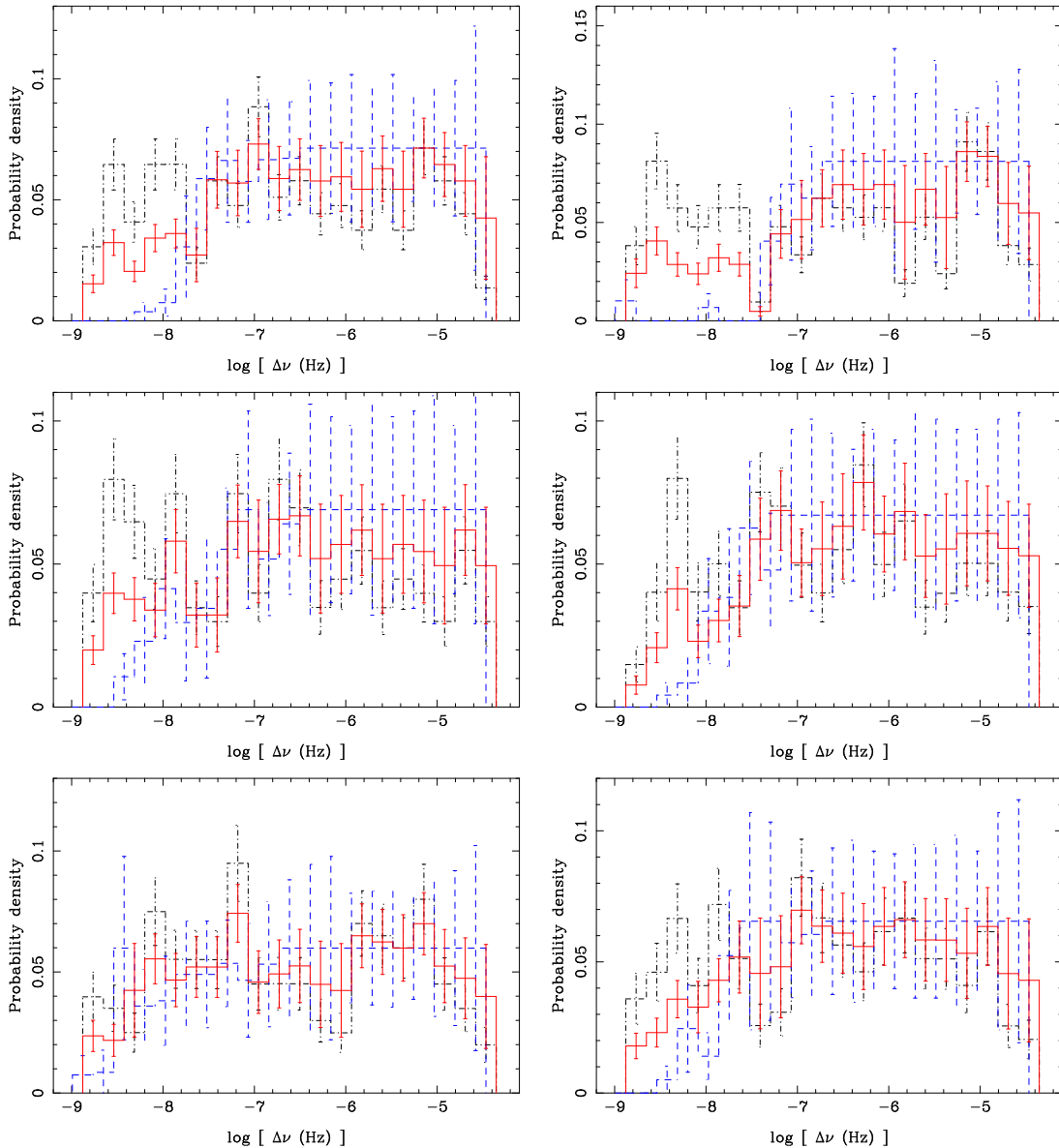


**Figure 8.** Glitch detection probability densities of PSRs J1048–5832 and J1413–6141 (first row), PSRs J1420–6048 and J1740–3015 (second row), PSRs J1801–2304 and J1801–2451 (third row). Blue dashed bars indicate the noise term, black dashed-dotted bars indicate the epoch and multi-glitch terms and red solid bars indicate the complete probability. Binning is the same as Figure 5. To present the histograms clearer, the black dashed-dotted and red solid bars are shifted right by half bin size.

the fairly large Yu et al. data sets. The probability for detecting a glitch event in pulsar timing observations is determined by the time of occurrence of the glitch relative to entire observing span and observing cadences, time of occurrence of preceding/subsequent glitches relative to observing cadences and the strength of timing noise. By implementing the Monte Carlo simulation with assuming glitches distribute uniformly, we derived numerical solution of the complete probability formula (equation 1) for the group case that contained 157 pulsars. Using the obtained detection probability densities and the observed distribution, we inferred the aggregated glitch size probability distribution embedded in the data. The inferred distribution is only a bit more massive than the observed distribution

for glitch sizes  $\lesssim 4 \times 10^{-7}$  Hz, implying Yu et al. have detected all detectable glitches in the data using the manual method and we have well modelled the detectabilities to glitches of the data sets and manual method. By implementing Monte Carlo simulations in the same way, we derived glitch detection probability densities for each of the seven pulsars with glitch numbers  $\geq 5$ . With inferring the glitch size distribution embedded in the data for the seven pulsars each, we compared the power-law model of the inferred distribution with that of the observed distribution. For PSRs J1048–5832, J1413–6141, J1420–6048, J1740–3015, J1801–2304 and J1801–2451, no significant differences were seen. The most prominent difference occurred for PSR J1341–6220, the power exponent  $s$  varied

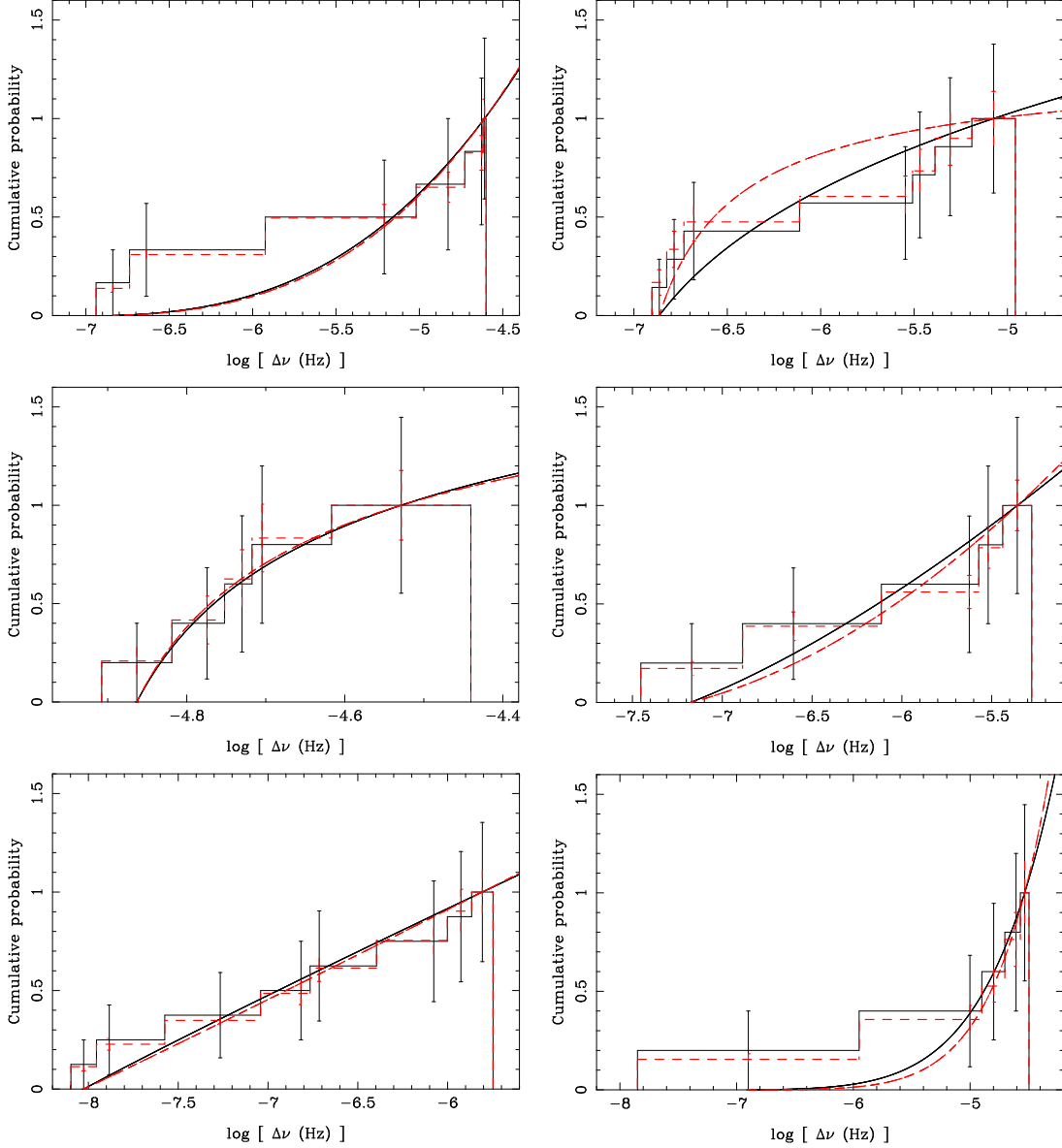


**Figure 9.** The observed (black solid) and inferred (red dashed) glitch size cumulative distributions for PSRs J1048–5832 and J1413–6141 (first row), PSRs J1420–6048 and J1740–3015 (second row), PSRs J1801–2304 and J1801–2451 (third row). Curves are the fitted power-law models (see Table 1 for parameters).

from the observed  $+0.7_{-0.7}^{+1.4}$  to the inferred  $-0.4_{-0.4}^{+1.0}$ . We suggest observers determine the glitch detection probability. It helps extract glitch distribution embedded in data and then plays a role in studying theoretical models e.g. the avalanche model (Warszawski & Melatos 2008; Melatos et al. 2008), the coherent noise model (Melatos & Warszawski 2009) and the Gross-Pitaevskii model (Warszawski & Melatos 2011). In addition, by deriving the Lomb normalised periodogram for the glitch time series observed in PSR J1341–6220, we found the power exponent  $b = 0.5(3)$  is not what flicker noise expects suggesting glitch phenomenon possesses different temporal characteristic from the self-organised criticality.

However, the seventeen glitches observed in PSR J1341–6220 are not adequate to fully charac-

terise the pulsar’s glitch temporal behaviour. More data are needed to measure the exponent  $b$  more accurately. Up till now, the power exponent  $s$  has only been measured for a few pulsars, intrinsic glitch size distribution has only been inferred for the Crab pulsar (Espinoza et al. 2014). Time scale of the rising edge of pulse frequency at glitch has only been measured for a few cases (e.g. Lyne et al. 1992; Wong et al. 2001; Dodson et al. 2002), it has not been adequate to study the distribution and correlation with glitch sizes. All of these require more observations especially those with high sensitivity instruments e.g. the Five-hundred-meter Aperture Spherical Telescope (FAST) and Square Kilometre Array (SKA).

**Table 1.** Parameters of the Kolmogorov-Smirnov tests for modelling the glitch size cumulative distributions of the seven pulsars with power-law functions. The columns give pulsar Jname, observed minimum and maximum glitch sizes, 68 per cent lower boundary, central value and 68 per cent upper boundary of the power exponent fitted for the observed distribution, 68 per cent false-alarm probability of the null hypothesis (the observed distribution and model are drawn from the same distribution), 68 per cent lower boundary, central value and 68 per cent upper boundary of the power exponent fitted for the inferred distribution, 68 per cent false-alarm probability of the null hypothesis (the inferred distribution and model are drawn from the same distribution).

PSR J	$\Delta\nu_{\min}$ (Hz)	$\Delta\nu_{\max}$ (Hz)	Observed				Inferred			
			$s_-$	$s$	$s_+$	$Q_{KS}$	$s_-$	$s$	$s_+$	$Q_{KS}$
J1048–5832	$10^{-6.838}$	$10^{-4.609}$	-2.8	1.9	14.1	0.300	-2.3	2.0	12.9	0.219
J1341–6220	$10^{-7.211}$	$10^{-5.073}$	0.0	0.7	2.1	0.147	-0.8	-0.4	0.6	0.095
J1413–6141	$10^{-6.864}$	$10^{-5.074}$	-5.9	-0.8	4.0	0.102	-8.3	-1.8	5.7	0.302
J1420–6048	$10^{-4.528}$	$10^{-4.863}$	-3.8	-1.3	0.8	0.001	-4.1	-1.4	0.5	0.017
J1740–3015	$10^{-7.177}$	$10^{-5.356}$	-3.4	0.5	13.1	0.021	-3.1	0.9	13.7	0.029
J1801–2304	$10^{-8.026}$	$10^{-5.806}$	-1.7	-0.1	2.6	0.002	-1.6	0.0	2.6	0.001
J1801–2451	$10^{-6.900}$	$10^{-4.532}$	-0.6	5.9	17.5	0.009	0.0	7.4	24.6	0.001

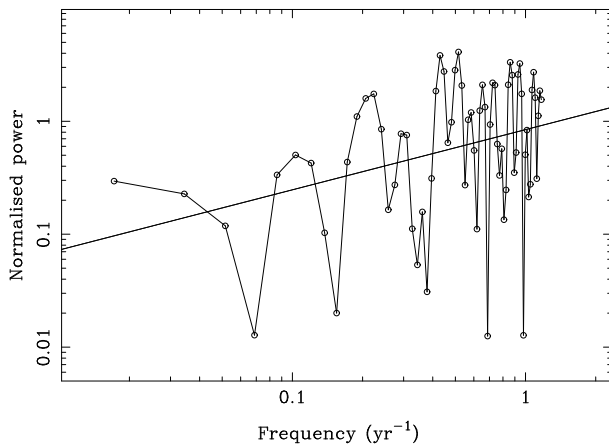


**Figure 10.** The Lomb normalised periodogram for the glitch time series observed in PSR J1341–6220. The straight line denotes the least-squares fit with  $y = -0.07(16) + 0.5(3)x$ .

## ACKNOWLEDGEMENTS

This work is supported by the National Natural Science Foundation of China (NSFC, No. 11403060), the Joint Research Fund in Astronomy (U1531246) under cooperative agreement between the NSFC and Chinese Academy of Sciences (CAS), the Strategic Priority Research Program ‘The Emergence of Cosmological Structures’ of the CAS (No. XDB09000000), the International Partnership Program of the CAS (No.114A11KYSB20160008) and the Strategic Priority Research Program of the CAS (No. XDB23000000).

MY acknowledges Dr. R. N. Manchester for commenting the manuscripts; Dr. G. Hobbs 1) for introducing software PTASIMULATE and TEMPONEST, 2) together with Dr. J. B. Wang for introducing the ‘pulse numbering’ operation in TEMPO2 and 3) for commenting the initial manuscript; Dr. L. Lentati for TEMPONEST set-up; Dr. K. J. Lee for helpful discussion. MY especially acknowledges the anonymous

referee for the comments which greatly helped in improving the paper both in science and English expression.

MY is extremely grateful to parents H. Q. He and G. C. Yu for their encouragement.

## REFERENCES

- Arzoumanian Z., Nice D. J., Taylor J. H., Thorsett S. E., 1994, *ApJ*, 422, 671
- Bak P., Tang C., Wiesenfeld K., 1988, *Phys. Rev. A*, 38, 364
- Coles W., Hobbs G., Champion D. J., Manchester R. N., Verbiest J. P. W., 2011, *MNRAS*, 418, 561
- D’Alessandro F., McCulloch P. M., Hamilton P. A., Deshpande A. A., 1995, *MNRAS*, 277, 1033
- Dodson R. G., McCulloch P. M., Lewis D. R., 2002, *ApJ*, 564, L85
- Edwards R. T., Hobbs G. B., Manchester R. N., 2006, *MNRAS*, 372, 1549
- Espinoza C. M., Antonopoulou D., Stappers B. W., Watts A., Lyne A. G., 2014, *MNRAS*, 440, 2755
- Espinoza C. M., Lyne A. G., Stappers B. W., Kramer M., 2011, *MNRAS*, 414, 1679
- Feroz F., Hobson M. P., Bridges M., 2009, *MNRAS*, 398, 1601
- Hobbs G., Lyne A. G., Kramer M., 2010, *MNRAS*, 402, 1027
- Hobbs G., Lyne A. G., Kramer M., Martin C. E., Jordan C., 2004, *MNRAS*, 353, 1311
- Hobbs G. B., Edwards R. T., Manchester R. N., 2006, *MNRAS*, 369, 655
- Janssen G. H., Stappers B. W., 2006, *A&A*, 457, 611
- Lentati L., Alexander P., Hobson M. P., Feroz F., van Haasteren R., Lee K. J., Shannon R. M., 2014, *MNRAS*, 437, 3004
- Liu K., Keane E. F., Lee K. J., Kramer M., Cordes J. M., Purver M. B., 2012, *MNRAS*, 420, 361
- Lomb N. R., 1976, *ASS*, 39, 447

- Lyne A. G., Graham-Smith F., Pritchard R. S., 1992, *Nature*, 359, 706
- Melatos A., Peralta C., Wyithe J. S. B., 2008, *ApJ*, 672, 1103
- Melatos A., Warszawski L., 2009, *ApJ*, 700, 1524
- Ransom S. M., Eikenberry S. S., Middleditch J., 2002, *AJ*, 124, 1788
- Scargle J. D., 1982, *ApJ*, 263, 835
- Warszawski L., Melatos A., 2008, *MNRAS*, 390, 175
- Warszawski L., Melatos A., 2011, *MNRAS*, 415, 1611
- Wong T., Backer D. C., Lyne A., 2001, *ApJ*, 548, 447
- Yu M., Manchester R. N., Hobbs G., Johnston S., Kaspi V. M., Keith M., Lyne A. G., Qiao G. J., Ravi V., Sarkissian J. M., Shannon R., Xu R. X., 2013, *MNRAS*, 429, 688
- Yuan J. P., Wang N., Manchester R. N., Liu Z. Y., 2010, *MNRAS*, 404, 289